Peculiar magnetism and magneto-transport properties in a non-centrosymmetric self-intercalated van der Waals ferromagnet Cr_5Te_8

Banik Rai[1], Sandip Kumar Kuila[2], Rana Saha[3,4], Chandan De[5,6], Sankalpa Hazra[7], Venkatraman Gopalan[5,7], Partha Pratim Jana[2], Stuart S. P. Parkin[3], Nitesh Kumar[1]

[1]S. N. Bose National Centre for Basic Sciences, Salt Lake City, Kolkata 700106, India

[2]Department of Chemistry, Indian Institute of Technology, Kharagpur 721302, India

[3]Max Planck Institute of Microstructure Physics, Weinberg 2, Halle (Saale) 06120, Germany

[4]Department of Chemistry, Indian Institute of Science Education and Research (IISER) Tirupati, Tirupati 517507, India

[5]Department of Physics, The Pennsylvania State University, University Park, PA, 16802, USA

[6]2D Crystal Consortium, Materials Research Institute, The Pennsylvania State University, University Park, PA, USA

[7]Department of Materials Science and Engineering, The Pennsylvania State University, University Park, PA 16802, USA

Abstract

Trigonal Cr_5Te_8, a self-intercalated van der Waals ferromagnet with an out of plane magnetic anisotropy, has long been known to crystallise in a centrosymmetric structure. Through detailed structural analysis together with second harmonic generation experiments, we show that the compound actually adopts a non-centrosymmetric structure. A large anomalous Hall conductivity of 102 $\Omega^{-1}\mathrm{cm}^{-1}$ at low temperature stems from intrinsic origin, which is larger than any previously reported values in bulk Cr-Te system. In addition, we observe a hump-like feature in the field-dependent Hall resistivity data, resembling a typical topological Hall signal. We demonstrate that the feature is highly tunable and is not related to topological Hall effect even though we observe Néel-type skyrmions by Lorentz transmission electron microscopy which is consistent with the non-centrosymmetric structure of the compound.

Introduction

Van der Waals (vdW) magnets have recently garnered considerable attention due to their potential technological applications.[1–3] Magnetic anisotropy can stabilize long-range magnetic ordering in such systems even in the monolayer limit.[1,2] Among vdW compounds, transition metal dichalcogenides (TMDs) are particularly noteworthy due to their diverse physical properties, spanning from narrow band gap semiconductors[4,5] to topological semimetals[6,7] and superconductors.[8] These systems also offer flexibility for controlled intercalation within the vdW gaps, leading to phenomena such as superconductivity,[9,10] chirality-induced topological Hall effect,[11] intrinsic anomalous Hall effect[12,13] etc. $CrTe_2$, in particular, has attracted particular attention because it is a rare example of vdW ferromagnetic TMD.[14–17] In the ultrathin limit, the magnetic easy axis of $CrTe_2$ is out-of-plane, which becomes in-plane as the thickness increases.[16] By intercalating additional Cr atoms into the vdW gaps, an out-of-plane magnetic easy axis can be achieved in bulk samples.[18] Cr_5Te_8 is one such self-intercalated compound which is known to exist in two distinct phases viz, trigonal (tr) Cr_5Te_8 and monoclinic (m) Cr_5Te_8.[19] These phases differ slightly in composition with the monoclinic phase being stable in the range of 59.6-61.5 at% Te, while the trigonal phase is stable in the range of 61.8-62.5 at% Te.[19] The Curie temperature of Cr_5Te_8 ranges from 180 K to 230 K and is highly susceptible to the amount of Cr intercalation. According to the available literature, tr-Cr_5Te_8 and m-Cr_5Te_8 crystallise in space groups $P\bar{3}m1$ and C2/m respectively,[19] both being centrosymmetric. In particular, topological Hall effect which stems from the scalar spin chirality (SSC),[20,21] has been observed in tr-Cr_5Te_8.[22] SSC is associated with a non-coplanar spatial arrangement of spins $\left(\chi_{ijk} = \boldsymbol{S}_i \cdot (\boldsymbol{S}_j \times \boldsymbol{S}_k)\right)$, often stabilised by the competition between the symmetric Heisenberg interaction (HI) and the antisymmetric Dzyaloshinskii-Moriya interaction (DMI), the latter being absent in centrosymmetric systems.[23,24] Furthermore, a DMI induced skyrmionic phase has been observed in Cr-rich $Cr_{1.3}Te_2$, where the crystal structure was found to be non-centrosymmetric.[25] This discrepancy underscores contradictory claims regarding the structure and thereby in their corresponding magnetic and electronic properties.

In this work we have investigated the crystal structure, magnetic and transport properties of tr-Cr_5Te_8. Through detailed single crystal and powder X-ray diffraction along with second harmonic generation (SHG) experiments we show that the compound crystallises in a non-centrosymmetric space group. In addition to the anomalous Hall effect, we have observed an anomaly in the magnetic field-dependent Hall resistivity data characterised by a hump-like feature near the magnetic saturation. We have tracked this feature in detail to understand whether it is anyway related the topological Hall effect stemming from the Néel-type skyrmions as observed using Lorentz transmission electron microscopy (LTEM).

Experimental Section

Single crystals of tr-Cr_5Te_8 were grown by the self-flux method. Pieces of Cr (99.99%, *Alfa Aesar*) and Te (99.999%, *Alfa Aesar*), in the molar ratio Cr : Te = 18 : 82, were taken in a quartz crucible and sealed in a quartz tube under vacuum. The tube was then placed in a muffle furnace, heated to 1273 K, held at this temperature for 10 h, and cooled slowly (2 K/h) to 1073 K. After being held at 1073 K for 34 h, the tube was immediately removed from the furnace and centrifuged to remove the excess flux. The result was large, lustrous single crystals as shown in Fig. 1(a).

The elemental ratio was checked using the energy dispersive X-ray spectroscopy (EDXS) technique. EDXS data were collected on a field emission scanning electron microscope (Quanta 250 FEG) equipped with an Element silicon drift detector (SDD) with an accelerating voltage of 25 kV and an accumulation time of 60 s. Single crystal X-ray diffraction (SCXRD) intensities were collected at room temperature using the BRUKER Photon II detector in the Bruker D8 Quest diffractometer equipped with Mo Kα (λ = 0.71073 Å) radiation. Apex 4 software was used for data acquisition and integration.[26] Precision images (Supp. Fig. S3) were constructed using CrysAlis Pro software.[27] Powder X-ray diffraction (PXRD) experiments were performed in the 2θ range of 10° to 140° at room temperature using a Rigaku SmartLab diffractometer equipped with a 9 kW Cu Kα (λ = 1.5418 Å) X-ray source. The reflection profiles of the PXRD were refined using the pseudo-Voigt function (4 parameters were used). March-Dollase function was used to handle the preferred orientation along [0001] direction. Berar-Baldinozzi correction (4 asymmetric parameters) was implied for asymmetric correction of the powder profile. Jana2006 software was used for both PXRD and SCXRD data refinement.[28,29] The orientation of single crystals was verified by X-ray Laue diffractometer in reflected geometry and the patterns were analysed by Orient Express software.

SHG measurements were performed using an 800-nm fundamental laser beam from a Spectra-Physics SOLSTICE ACE Ti: sapphire laser (pulse width ~80 fs, repetition rate of 1 kHz). A half-wave retarder plate was used to control the incident polarization of the fundamental beam. The generated second-harmonic light was first spectrally filtered, and then decomposed to two orthogonal components by an analyser and finally detected by a photomultiplier tube. SHG polar plots were measured corresponding to these two orthogonal components of generated SHG as a function of the polarization of the incident fundamental light. All SHG measurements were done in reflection geometry with a 45° incidence angle.

For transmission electron microscopy (TEM) investigations lamellae were prepared from the single crystal of tr-Cr_5Te_8 using the focused ion beam (FIB) Ga+ ion milling technique. This process was carried out with an FEI Nova Nanolab 600 SEM/FIB system operating at 30 keV ion-beam energy, utilizing standard lift-out procedures. Subsequent polishing of the lamellae was performed at lower Ga+ ion-beam energies (5 keV) to minimize the thickness of any amorphous surface layers. High-resolution TEM (HRTEM) imaging was conducted utilizing the JEOL ARM300F2 TEM. Magnetic textures were imaged using a JEOL JEM-F200 TEM operating in Lorentz mode at an acceleration voltage of 200 keV. A GATAN double-tilt sample holder capable of varying the temperature between 100 K and 380 K was employed for these experiments. To apply a vertical magnetic field to the lamella within the TEM column, currents were passed through the coils of the objective lens. Imaging was facilitated using a Lorentz mini-lens.

A standard six-terminal method was employed to measure both the longitudinal resistivity ρ_{xx} and transverse Hall resistivity ρ_{yx} at simultaneously different temperatures and magnetic fields. The current was applied in the *ab*-plane and the magnetic field along the *c*-axis of the crystal sample. Magnetic measurements were carried out using the VSM (Vibrating Sample Magnetometer) option of the Physical Properties Measurement System (PPMS, DynaCool, Quantum Design, 9T). Electrical transport measurements were also carried out in PPMS, using its ETO (Electrical Transport Option) option.

Results and discussions

The elemental composition as verified by EDXS [Supp. Table S1] is 38.06 at% Cr and 61.94 at% Te ($Cr_{4.92}Te_8$), which is within the homogeneity range of tr-Cr_5Te_8.[19] Fig. 1(a) shows the as-grown single crystals of tr-Cr_5Te_8, each measuring several millimetres in size. Laue diffraction pattern captured in the reflected mode along the *c*-axis of the crystal is shown in Fig. 1(b). The pattern consists of three-fold symmetric points (highlighted by red arrows), confirming the trigonal structure of tr-Cr_5Te_8. The high-resolution transmission electron microscopy (HRTEM) image depicted in Fig. 1(c), taken along the $[10\bar{1}0]$ direction, clearly illustrates the layered structure of tr-Cr_5Te_8 along the [0001] direction. The existing literature on tr-Cr_5Te_8 suggests that it adopts the centrosymmetric space group $P\bar{3}m1$. We therefore started the refinement of the SCXRD data by considering this model. The structure solution (performed using Superflip in Jana2006)[28,29] using the $P\bar{3}m1$ space group yielded seven independent crystallographic sites, of which four are Te sites (Te1, Te2, Te3, Te4) and three are Cr sites (Cr1, Cr2, Cr3). A detailed step-by-step description of the structure refinement process is discussed in the Supplementary Information. Details of the structure solution and refinement using the $P\bar{3}m1$ space group are tabulated in Tables 1 & 2.

Table 1: Data collection and single crystal refinement details of tr-Cr_5Te_8.

Nominal Composition	Cr_5Te_8 (S1)	Cr_5Te_8 (S2)
Chemical formula	$Cr_{4.885}Te_8$	$Cr_{4.876}Te_8$
M_r	1274.8	1274.3
Pearson symbol	$hP28$	
Crystal system, space group	Trigonal, $P\bar{3}m1$	Trigonal, $P3m1$
Temperature (K)	297(2)	
a, c (Å)	7.8153(3), 11.9807(3)	
V (Å^3)	633.73(4)	
Z	2	
Radiation type	Mo Kα	
μ (mm^{-1})	22.06	22.05
Crystal size (mm)	0.14 × 0.11 × 0.04	
Data collection		
Diffractometer	Bruker Photon II	
Absorption correction	multi-scan	
T_{min}, T_{max}	0.419, 0.748	
No. of measured, independent and observed [$I > 3\sigma(I)$] reflections	19982, 1184, 828	19982, 2356, 1521
R_{int}	0.054	0.042
$(\sin \theta/\lambda)_{max}$ (Å^{-1})	0.833	
Refinement		
R [$F^2 > 2\sigma(F^2)$]	0.025	0.035
$wR(F^2)$ (all data)	0.105	0.128
GOF (all data)	1.83	1.70
No. of reflections	1184	2356
No. of parameters	37	67

Nominal Composition	Cr_5Te_8 (S1)	Cr_5Te_8 (S2)
$\Delta\rho_{max}$, $\Delta\rho_{min}$ (e.Å^{-3})	1.79, -1.64	1.37, -1.57

Table 2: Coordinates, site occupancy factor and isotropic displacement parameters of tr-Cr_5Te_8 ($P\overline{3}m1$, $hP28$, 164).

Atom	Wyck.	Site	S.O.F.	*x/a*	*y/b*	*z/c*	*U* [Å^2]
Te1	2*d*	3*m*.	1	1/3	2/3	0.88347(4)	0.01141(13)
Te2	2*d*	3*m*.	1	2/3	1/3	0.63090(4)	0.01033(13)
Te3	6*i*	.*m*.	1	0.16702(1)	0.33404(2)	0.62107(2)	0.01109(12)
Te4	6*i*	.*m*.	1	0.83273(1)	0.16727(1)	0.87389(2)	0.01075(12)
Cr1	1*a*	-3*m*.	0.891(6)	0	0	0	0.0077(3)
Cr2	2*c*	3*m*.	1	0	0	0.25471(8)	0.0115(2)
Cr3	6*i*	.*m*.	1	0.50680(4)	0.49320(4)	0.24871(5)	0.0113(2)
Cr4	3*f*	.2/*m*.	0.293(4)	1/2	0	1/2	0.0143(10)

In a recent report, the structure of $Cr_{1.3}Te_2$ was reported to be non-centrosymmetric with space group $P3m1$.[25] To check the validity of the non-centrosymmetric space group, the symmetry of the structural model was reduced from $P\overline{3}m1$ (S1) (CCDC: 2343363) to $P3m1$ (S2) (CCDC: 2343364), which is also prompted due to a group-subgroup relationship between these two space groups (Supp. Fig. S9). The newly generated structure parameters were then refined and compared with the original $P\overline{3}m1$ model. Due to the reduction in symmetry, a total of fourteen sites were generated from eight sites. Each tellurium site (Te1, Te2, Te3 and Te4) was split into two sites. Two of the four chromium sites (Cr2 and Cr3) were split into four sites (Cr2_1, Cr2_2, Cr3_1 and Cr3_2). The refinement parameters in this structure model are slightly better in favour of space group $P3m1$. The refinement results are given in Tables 1 & 3.

Table 3: Coordinates, site occupancy factor and isotropic displacement parameters of tr-Cr_5Te_8 ($P3m1$, $hP28$, 156).

Atom	Wyck.	Site	S.O.F.	*x/a*	*y/b*	*z/c*	*U* [Å^2]
Te1_1	1*b*	3*m*.		1/3	2/3	0.88342(10)	0.0103(4)
Te1_2	1*c*	3*m*.		-1/3	-2/3	-0.88362(12)	0.0126(4)
Te2_1	1*c*	3*m*.		2/3	1/3	0.63092(12)	0.0119(4)
Te2_2	1*b*	3*m*.		-2/3	-1/3	-0.63091(12)	0.0091(4)
Te3_1	3*d*	.*m*.		0.16681(6)	0.33361(11)	0.62090(9)	0.0115(3)
Te3_2	3*d*	.*m*.		-0.16724(6)	-0.33447(11)	-0.62130(8)	0.0110(3)
Te4_1	3*d*	.*m*.		0.83284(6)	0.16716(6)	0.87376(10)	0.0094(2)
Te4_2	3*d*	.*m*.		-0.83263(6)	-0.16736(6)	-0.87420(9)	0.0125(3)

Cr1	1*a*	3*m*.	0.883(5)	0	0	0.0015(7)	0.0075(3)
Cr2_1	1*a*	3*m*.		0	0	0.2545(4)	0.0118(8)
Cr2_2	1*a*	3*m*.		0	0	-0.2547(5)	0.0126(9)
Cr3_1	3*d*	.*m*.		0.50700(16)	0.49300(16)	0.2489(4)	0.0128(6)
Cr3_2	3*d*	.*m*.		-0.50669(16)	-0.49331(16)	-0.2483(4)	0.0108(5)
Cr4	3*d*	.*m*.	0.289(4)	0.5035(8)	0.0071(16)	0.5029(9)	0.0115(12)

Fig. 1(c) shows the PXRD data fitted with $P3m1$ (S2) space group using the Rietveld refinements. The refinement parameters are given in the figure caption. A good fit can be obtained with the space group $P\bar{3}m1$ (S1) as well with almost similar fitting parameters (see Supp. Information). Therefore, it is difficult to determine conclusively whether the crystal adopts the centrosymmetric $P\bar{3}m1$ (S1) or non-centrosymmetric $P3m1$ (S2) space group based on the XRD data alone.

To address this uncertainty, we have performed second harmonic generation (SHG) experiments. Fig. 2(a) schematic of the SHG setup used. SHG is a frequency doubling non-linear optical process where two photons at the fundamental frequency (ω) generate a photon of twice the frequency (2ω).[30] Only non-centrosymmetric materials are SHG active, making SHG an excellent probe for detecting evidence of broken inversion symmetry. Fig. 2(b) shows the measured SHG polar plots as a function of incident polarization of fundamental beam from tr-Cr_5Te_8 single crystal, signifying the non-centrosymmetric structure of the crystal.

The induced second harmonic polarization ($\boldsymbol{P^{2\omega}}$) in any material depends on the incident fundamental electric field ($\boldsymbol{E^{\omega}}$) through the nonlinear susceptibility tensor (d_{ijk}) as $\boldsymbol{P_i^{2\omega}} \propto d_{ijk}\boldsymbol{E_j^{\omega}}\boldsymbol{E_k^{\omega}}$. Here, ($i,j,k$) refer to the lab coordinate system (X, Y, Z) which are tied to the crystal axes of tr-Cr_5Te_8 : ($X\,||[10\bar{1}0]$, $Y\,||[01\bar{1}0], \mathrm{Z}\,||\,[0001]$). The incident electric field, $\boldsymbol{E^{\omega}}$, can be written as $\boldsymbol{E_{\omega}} = (E_{\omega}\cos(\varphi), E_{\omega}\sin(\varphi), 0)$ (φ is the angle of the polarization as shown in Fig. 2(a)-(b)).

For point group $3m$, d_{ijk} can be written in Voight notation as follows:[30]

$$d_{ij} = \begin{pmatrix} 0 & 0 & 0 & 0 & d_{15} & -d_{22} \\ -d_{22} & d_{22} & 0 & d_{15} & 0 & 0 \\ d_{31} & d_{31} & d_{33} & 0 & 0 & 0 \end{pmatrix}$$

From this the expected SHG intensity for two orthogonal directions (X and Y) can be calculated as follows for the case 45° oblique incidence angle of the fundamental beam:

$$I_X^{2\omega} \propto (P_X^{2\omega})^2 \propto \left((2d_{15} - d_{31} - d_{33})\cos{[\varphi]}^2 - 2d_{31}\sin{[\varphi]}^2 + \sqrt{2}d_{22}\mathrm{Sin}\,[2\varphi]\right)^2$$

$$I_Y^{2\omega} \propto (P_Y^{2\omega})^2 \propto (d_{22} - 3d_{22}\mathrm{Cos}\,[2\varphi] - 2\sqrt{2}d_{15}\sin{[2\varphi]})^2$$

The proportionality constants depend on the absolute fluence of the laser and Fresnel coefficients for the air-sample interface. These equations can be used to fit the measured polar plots confirming the observation of $3m$ symmetry in tr-Cr_5Te_8.

The XRD and SHG experiments together confirms that tr-Cr_5Te_8 crystallises in the non-centrosymmetric space group $P3m1$ (S2) with 14 different crystallographic sites with the cell parameters a = 7.8153(3) Å, c = 11.9807(3) Å. The six independent crystallographic sites are occupied by Cr atoms, while the remaining eight crystallographic sites are occupied by Te atoms [Fig. 2(a)]. The structure can be viewed as a stuffed CdI_2 type structure [Fig. 2(b)]. The split Cr sites (Cr2_1, Cr2_2, Cr3_1 and Cr3_2) are surrounded by six Te atoms to form $CrTe_6$ octahedra. Cr2_1 and Cr2_2 centred octahedra are linked together by edge-sharing to form a CdI_2-type slab. Similarly, another CdI_2 type slab is formed by the edge sharing of Cr3_1 and Cr3_2-centered octahedra. These slabs are alternately stacked along the [0001] direction. The other two partially occupied Cr atoms (Cr1 and Cr4) are located in octahedral interstices and alternate between two adjacent slabs.

The temperature dependent magnetisation (*M-T* curve), with $H = 0.1$ T applied along the *c*-axis, shown in Fig. 3(a), indicates that tr-Cr_5Te_8 undergoes a ferromagnetic (FM) ordering with a Curie Temperature (T_C) ~ 200 K. A clear bifurcation is observed between the FC and ZFC curves as the temperature is lowered, indicating a significant magnetocrystalline anisotropy in tr-Cr_5Te_8. When the same field is applied in the *ab*-plane [Supp. Fig. S6(a)], the magnetization value decreases by almost an order of magnitude and its variation with temperature, $M(T)$, looks more like an antiferromagnetic *M-T* curve, suggesting a possible canting of magnetic spins away from the *c*-axis.

The magnetic field dependent magnetisation (*M-H* curve) at temperature 2 K with the magnetic field applied along the *c*-axis in the range of $\pm$ 1 T is shown in Fig. 3(b). The magnetisation saturates at the field H_S ~ 0.3 T and the value of the saturation magnetisation is $M_S \sim 2\ \mu_B/\mathrm{Cr}$, which is in agreement with the reported values.[31-33] The appearance of a hump-like feature on either side of the *M-H* curve is what makes the curve interesting. When the field is reduced from 1 T (-1 T), the magnetisation does not follow the typical path near H_S ($-H_S$) and remains saturated up to a critical field ~ 0.17 T (-0.17 T). At this critical field, the magnetisation undergoes a sudden, sharp drop, after which it returns to its usual path. This anomaly in the magnetisation has been observed previously also in $Cr_{1+d}Te_2$ compounds[34,35] as well as in compounds such as $BaFe_{10}O_{19}$,[36] Fe_3GeTe_2,[37] $PrMn_2Ge_2$,[38] $Mn_{1.4}PtSn$[39] etc. In particular, in $BaFe_{10}O_{19}$ and $Mn_{1.4}PtSn$, the evolution of magnetic domains in the external magnetic field has been observed using magnetic force microscopy and magneto-optical Kerr microscopy, respectively. Direct observation of domain evolution is consistent with the appearance of humps in the *M-H* curve, but does not explain why the humps should appear in the first place. To investigate this anomaly further, we repeated the measurements in the field range of $\pm$8 T, $\pm$7 T, $\pm$6 T, $\pm$5 T and $\pm$0.4 T [Fig. 3(c)]. The humps continue to appear for lower field ranges up to the $\pm$6 T range, appearing only on the positive side for the $\pm$0.5 T range and disappearing completely for the $\pm$0.4 T range. This suggests that $\pm$0.5 Tis the critical range of the magnetic field above which the humps begin to appear and below which they do not. The *M-H* curve for the $\pm$0.5 range, has its own peculiarity. The appearance of a hump on only one side of the *M-H* curve is unprecedented. To further investigate this peculiarity, we cooled the sample from the paramagnetic state to 2 K without applying any magnetic field, to eliminate any possible magnetic history, and performed a series of hysteresis cycles at 2 K. As shown in Fig. 3(d), the initial (virgin) curve now has a hump on both sides of the curve, whereas the subsequent curves only have a hump on the positive side. This demonstrates that the magnetic history can affect the appearance of the humps. Since $\pm$0.5 T is the critical range of the magnetic field for their appearance, any magnetic history in the sample could favour the hump to one side. This is better illustrated in Fig. 3(e). The magnetic hysteresis, coloured in red (blue), was measured in the field range of $\pm$0.5 T on the sample initially exposed to a magnetic field of 1 T (-1 T). The red (blue) curve shows a clear bias of the hump to the positive (negative) side of the *M-H* curve.

To investigate the nature of magnetic domain in tr-Cr_5Te_8, LTEM experiments were performed on a thin *c*-axis oriented lamella of the compound. LTEM images were taken at a defocus value of 1.5 mm at zero magnetic field after cooling the sample from room temperature to 100 K in a magnetic field of 100 Oe. Sharp circular features, indicative of magnetic textures, were observed when the lamella was slightly tilted away from the electron beam during the observation. The tilt angles α (about X-axis), β (about Y-axis), and the corresponding tilt axes are defined in Fig. 5(a). The circular features show dark and bright contrasts along their opposite edges. A reversal of the contrasts was observed for both tilt axes when the lamella was tilted in the opposite direction, i.e., the contrasts were reversed for +α (+β) and -α (-β) tilts. Fig. 5(b)-5(e) shows the LTEM images taken at a tilt angle of $\pm$15° about the X- and Y-axes. A clear 90° contrast-rotation was also observed between the α- and β-tilt images. These observations, which are key identifying features of Néel-type skyrmions,[25,40-42] suggest that the magnetic textures in tr-Cr_5Te_8 is of Néel-type. However, the skyrmions do not form a regular lattice of the underlying crystal symmetry, suggesting that in addition to the DMI, a significant long-range dipolar interaction plays an important role in stabilising them. The skyrmions observed in tr-Cr_5Te_8 are similar to those observed in $Cr_{1.3}Te_2$, suggesting that these two phases are not very different magnetically.[25]

Fig. 6(a) shows the temperature dependence of the longitudinal resistivity (ρ_{xx}-T curve) from temperature 2 K to 300 K. The behaviour of ρ_{xx} is metallic throughout the temperature range with a residual resistivity ratio $RRR = \rho_{\mathrm{xx}}(300\ \mathrm{K})/\rho_{\mathrm{xx}}(2\ \mathrm{K}) \approx 3$. A clear anomaly corresponding to the ferromagnetic to paramagnetic phase transition is seen around 200 K, which is in good agreement with the M-T data. Fig. 6(b) shows the field-dependent Hall resistivity (ρ_{yx}-H curve) at different temperatures with the magnetic field applied along the c-axis. In a ferromagnetic material, the Hall resistivity ρ_{yx} generally consists of contributions from the ordinary Hall effect (OHE), arising from the magnetic Lorentz force acting on the moving charges and the anomalous Hall effect (AHE), arising from the extrinsic scattering processes and/or the intrinsic momentum space Berry curvature mechanism.[43] In certain materials, where a non-coplanar spin structure gives rise to a non-zero scalar spin chirality, an additional contribution, arising from the real space Berry curvature mechanism, called the topological Hall effect (THE), is expected in the Hall resistivity.[20,21] All these three contributions are expressed in the following empirical formula

$$\begin{aligned}\rho_{\mathrm{yx}} &= \rho_{\mathrm{yx}}^{\mathrm{OHE}} + \rho_{\mathrm{yx}}^{\mathrm{AHE}} + \rho_{\mathrm{yx}}^{\mathrm{THE}} \\ &= \mu_0 R_0 H + \mu_0 R_{\mathrm{S}} M + \rho_{\mathrm{yx}}^{\mathrm{THE}}\end{aligned}$$

where, $\rho_{\mathrm{yx}}^{\mathrm{OHE}}$, $\rho_{\mathrm{yx}}^{\mathrm{AHE}}$, $\rho_{\mathrm{yx}}^{\mathrm{THE}}$ are the ordinary, anomalous, and topological Hall resistivities, respectively. R_0 and R_{S} are the ordinary and anomalous Hall coefficients, respectively. The values of R_0 and $\rho_{\mathrm{yx}}^{\mathrm{AHE}}$ are given by the slope and the intercept of the linear fit of the ρ_{xy}-H curve in the saturation region. R_S can be calculated from the equation $\rho_{\mathrm{yx}}^{\mathrm{AHE}} = \mu_0 R_S M_{\mathrm{S}}$ where M_{S} can be taken from the M-H curves. Fig. 6(c) shows the variation of the anomalous Hall conductivity (AHC) $\sigma_{\mathrm{xy}}^{\mathrm{AHE}} \left(\frac{\rho_{\mathrm{yx}}^{\mathrm{AHE}}}{\rho_{\mathrm{xx}}^2+\rho_{\mathrm{yx}}^2} \approx \frac{\rho_{\mathrm{yx}}^{\mathrm{AHE}}}{\rho_{\mathrm{xx}}^2}\right)$ with temperature. AHC remains almost constant at low temperatures with a maximum value of $102\ \Omega^{-1}\mathrm{cm}^{-1}$ at 50 K. This value of AHC is higher than those previously reported in $Cr_{1+d}Te_2$ systems.[32,44] The drop in the value of AHC at higher temperatures can be attributed to the similar drop observed in the temperature dependence of the saturation magnetisation M_{S}. Thus, the variation of AHC with temperature is effectively negligible. This suggests that the intrinsic Karpus-Luttinger (KL) mechanism could be responsible for the AHE in tr-Cr_5Te_8, although previous reports have attributed the origin of the AHE to the extrinsic skew scattering mechanism.[32,44] The actual mechanism of the AHE can be determined by looking at the scaling nature of $\rho_{\mathrm{yx}}^{\mathrm{AHE}}$ with ρ_{xx}. In particular, a linear scaling of $\rho_{\mathrm{yx}}^{\mathrm{AHE}}$ with ρ_{xx}^{2} suggests either an intrinsic KL or an extrinsic side jump mechanism of the AHE whereas a linear scaling of $\rho_{\mathrm{yx}}^{\mathrm{AHE}}$ with ρ_{xx} suggests an extrinsic skew scattering mechanism of the AHE.[42] In Fig. 6(d) the normalised anomalous Hall resistivity, $\rho_{\mathrm{yx}}^{\mathrm{AHE}}/M_{\mathrm{S}}$, is plotted against ρ_{xx}^{2} and the points are fitted well with a linear line, implying an intrinsic KL mechanism of AHE. We rule out the existence of side jump effect because it is normally observed in bad metals. In Fig. 7, We have presented the logarithmic plot of $\sigma_{\mathrm{xy}}^{\mathrm{AHE}}$ vs σ_{xx} for tr-Cr_5Te_8, juxtaposed with data from other recognised AHE systems found in the literature.[45-54]

Although skyrmions are expected to generate an additional contribution, $\rho_{\mathrm{yx}}^{\mathrm{THE}}$, to the Hall resistivity through Berry curvature mechanisms,[55-57] we did not observe any such obvious signal in our measurements. In the absence of THE, the shape of the Hall resistivity mimics that of the magnetisation weighted by a constant slope arising from the OHE. The THE, if present, manifests itself in ρ_{yx}-H curve as a deviation from the shape of *M-H* curve. Thus, any feature in ρ_{yx}-H curve that is absent in *M-H* curve can, in principle, be attributed to THE. Fig. 7(a) and Fig. 7(b) show the field dependent Hall resistivities measured at 2 K following the same protocol as for the magnetisation measurements, i.e. the sample was first exposed to a magnetic field of 1 T and -1 T in Fig. 6(a) and Fig. 6(b) respectively, before measuring the hysteresis in the field range of ± 0.5 T. Interestingly, the hump-like features in ρ_{yx}-H curves mimic those observed in *M-H* curves. The Hall resistivity can be accurately modelled by a combined contribution from the OHE and the AHE ($\rho_{\mathrm{yx}}^{\mathrm{OHE}} + \rho_{\mathrm{yx}}^{\mathrm{AHE}}$). The difference between the experimental data and the fitted curve is almost flat everywhere, except for sharp peaks at the field values where the humps disappear. These peaks emerge because of the inconsistencies in the size of the hump in each measurement [Supp Fig. S7] and should not be attributed to the THE. To further verify that the ρ_{yx}-H curves accurately mimic the *M-H* curves, the Hall resistivity measured at 2 K in the field range of ± 1 T is fitted with the same model $\rho_{\mathrm{yx}} = \rho_{\mathrm{yx}}^{\mathrm{OHE}} + \rho_{\mathrm{yx}}^{\mathrm{AHE}}$ and is presented in Fig. 7(c). Again, the difference between the experimental data and the fitted curve remains largely flat, except for similar peaks arising from similar reasons. Thus, our measurements do not reveal any THE in tr-Cr_5Te_8, although we observe Néel type skyrmions in this system. A plausible explanation for this discrepancy can be given in terms of the difference in the dimensionality of the sample used in different experiments. The magnetotransport measurements were carried out on a bulk single crystal with a typical size of 3 × 1 × 0.3 mm, while the LTEM experiments were performed on a thin lamella with a typical thickness of 100 nm. Since, the dipolar interaction plays an important role in stabilising the skyrmion phase in tr-Cr_5Te_8, the size and stability of the skyrmions depend on the thickness of the sample. In particular, it has been found that in skyrmionic systems where dipolar interaction plays a crucial role in stabilizing the skyrmions, the size of skyrmions tends to grow with increasing thickness.[25,42,58-60] Since the size of the skyrmions cannot be increased indefinitely the skyrmionic phase becomes destabilised with increasing thickness, leading to the emergence of topologically trivial phases such as magnetic stripe domains as the thickness increases. Considering the similar case is true for tr-Cr_5Te_8, the skyrmion phase in a bulk sample is unstable. Since, the strength of THE is directly proportional to the skyrmion density,[61] we do not observe any THE in a bulk tr-Cr_5Te_8.

Conclusion

In summary, we have studied the crystal structure of tr-Cr_5Te_8 in detail through single crystal and powder X-ray diffraction experiments. The compound is found to crystallise in a non-centrosymmetric space group $P3m1$, rather than the previously reported centrosymmetric $P\overline{3}m1$, which is further confirmed by the second harmonic generation experiments. A large anomalous Hall conductivity of 102 $\Omega^{-1}\mathrm{cm}^{-1}$ at 50 K is observed, which originates from the intrinsic Karpus-Luttinger mechanism rather than the previously reported extrinsic skew scattering mechanism. An anomaly characterised by a hump-like feature is observed in the field dependent Hall resistivity data. These humps exactly mimic the similar humps observed in the field dependent magnetisation data, suggesting their magnetic origin. We have provided a protocol to deliberately induce this hump on one side of the magnetisation or Hall resistivity data. We have also observed Néel type skyrmions in tr-Cr_5Te_8 by Lorentz transmission electron microscopy, which are found to be stable even in the zero magnetic field.

Accession codes:

CCDC 2343363-2343364 contains the supplementary crystallographic information for this paper. These data can be obtained free of charge via www.ccdc.cam.ac.uk/data_request/cif, or by emailing data_request@ccdc.cam.ac.uk, or by contacting The Cambridge Crystallographic Data Centre, 12 Union Road, Cambridge CB2 1EZ, UK; fax: +44 1223336033.

Acknowledgements

NK acknowledges the Science and Engineering Research Board (SERB), India, for financial support through Grant Sanction No. CRG/2021/002747 and Max Planck Society for funding under Max Planck-India partner group project. SH, and VG acknowledge support from the Department of Energy Basic Sciences Division grant number DE-SC0012375 for the nonlinear optical characterization. PPJ would like to thank SERB, India (grant no. CRG/2020/004115), for financial support. SKK acknowledges the CSIR for research fellowship. This research project made use of the instrumentation facility provided by the Technical Research Centre (TRC) at the S. N. Bose National Centre for Basic Sciences, under the Department of Science and Technology, Government of India.

References

(1) Huang, B.; Clark, G.; Navarro-Moratalla, E.; Klein, D. R.; Cheng, R.; Seyler, K. L.; Zhong, Di.; Schmidgall, E.; McGuire, M. A.; Cobden, D. H.; Yao, W.; Xiao, D.; Jarillo-Herrero, P.; Xu, X. Layer-Dependent Ferromagnetism in a van Der Waals Crystal down to the Monolayer Limit. *Nature* **2017**, *546*, 270–273.

(2) Gong, C.; Li, L.; Li, Z.; Ji, H.; Stern, A.; Xia, Y.; Cao, T.; Bao, W.; Wang, C.; Wang, Y.; Qiu, Z. Q.; Cava, R. J.; Louie, S. G.; Xia, J.; Zhang, X. Discovery of Intrinsic Ferromagnetism in Two-Dimensional van Der Waals Crystals. *Nature* **2017**, *546*, 265–269.

(3) Fei, Z.; Huang, B.; Malinowski, P.; Wang, W.; Song, T.; Sanchez, J.; Yao, W.; Xiao, D.; Zhu, X.; May, A. F.; Wu, W.; Cobden, D. H.; Chu, J. H.; Xu, X. Two-Dimensional Itinerant Ferromagnetism in Atomically Thin Fe_3GeTe_2. *Nature Mater* **2018**, *17*, 778–782.

(4) Mak, K. F.; Shan, J. Photonics and Optoelectronics of 2D Semiconductor Transition Metal Dichalcogenides. *Nature Photon* **2016**, *10*, 216–226.

(5) Wang, Q. H.; Kalantar-Zadeh, K.; Kis, A.; Coleman, J. N.; Strano, M. S. Electronics and Optoelectronics of Two-Dimensional Transition Metal Dichalcogenides. *Nature Nanotech* **2012**, *7*, 699–712.

(6) Jiang, J.; Liu, Z. K.; Sun, Y.; Yang, H. F.; Rajamathi, C. R.; Qi, Y. P.; Yang, L. X.; Chen, C.; Peng, H.; Hwang, C. C.; Sun, S. Z.; Mo, S. K.; Vobornik, I.; Fujii, J.; Parkin, S. S. P.; Felser, C.; Yan, B. H.; Chen, Y. L. Signature of Type-II Weyl Semimetal Phase in $MoTe_2$. *Nat Commun* **2017**, *8*, 13973.

(7) Soluyanov, A. A.; Gresch, D.; Wang, Z.; Wu, Q.; Troyer, M.; Dai, X.; Bernevig, B. A. Type-II Weyl Semimetals. *Nature* **2015**, *527*, 495-498.

(8) Qi, Y.; Naumov, P. G.; Ali, M. N.; Rajamathi, C. R.; Schnelle, W.; Barkalov, O.; Hanfland, M.; Wu, S. C.; Shekhar, C.; Sun, Y.; Süß, V.; Schmidt, M.; Schwarz, U.; Pippel, E.; Werner, P.; Hillebrand, R.; Förster, T.; Kampert, E.; Parkin, S.; Cava, R. J.; Felser, C.; Yan, B.; Medvedev, S. A. Superconductivity in Weyl Semimetal Candidate $MoTe_2$. *Nat Commun* **2016**, *7*, 11038.

(9) Morosan, E.; Zandbergen, H. W.; Dennis, B. S.; Bos, J. W. G.; Onose, Y.; Klimczuk, T.; Ramirez, A. P.; Ong, N. P.; Cava, R. J. Superconductivity in Cu_xTiSe_2. *Nat Phys* **2006**, *2*, 544–550.

(10) Wagner, K. E.; Morosan, E.; Hor, Y. S.; Tao, J.; Zhu, Y.; Sanders, T.; McQueen, T. M.; Zandbergen, H. W.; Williams, A. J.; West, D. V.; Cava, R. J. Tuning the Charge Density Wave and Superconductivity in Cu_xTaS_2. *Phys. Rev. B* **2008**, *78*, 104520.

(11) Takagi, H.; Takagi, R.; Minami, S.; Nomoto, T.; Ohishi, K.; Suzuki, M. T.; Yanagi, Y.; Hirayama, M.; Khanh, N. D.; Karube, K.; Saito, H.; Hashizume, D.; Kiyanagi, R.; Tokura, Y.; Arita, R.; Nakajima, T.; Seki, S. Spontaneous Topological Hall Effect Induced by Non-Coplanar Antiferromagnetic Order in Intercalated van Der Waals Materials. *Nat Phys* **2023**, *19*, 961–968.

(12) Ghimire, N. J.; Botana, A. S.; Jiang, J. S.; Zhang, J.; Chen, Y. S.; Mitchell, J. F. Large Anomalous Hall Effect in the Chiral-Lattice Antiferromagnet $CoNb_3S_6$. *Nat Commun* **2018**, *9*, 3280.

(13) Park, P.; Cho, W.; Kim, C.; An, Y.; Kang, Y. G.; Avdeev, M.; Sibille, R.; Iida, K.; Kajimoto, R.; Lee, K. H.; Ju, W.; Cho, E. J.; Noh, H. J.; Han, M. J.; Zhang, S. S.; Batista, C. D.; Park, J. G. Tetrahedral Triple-Q Magnetic Ordering and Large Spontaneous Hall Conductivity in the Metallic Triangular Antiferromagnet $Co_{1/3}TaS_2$. *Nat Commun* **2023**, *14*, 8346.

(14) Zhang, X.; Lu, Q.; Liu, W.; Niu, W.; Sun, J.; Cook, J.; Vaninger, M.; Miceli, P. F.; Singh, D. J.; Lian, S. W.; Chang, T. R.; He, X.; Du, J.; He, L.; Zhang, R.; Bian, G.; Xu, Y. Room-Temperature Intrinsic Ferromagnetism in Epitaxial $CrTe_2$ Ultrathin Films. *Nat Commun* **2021**, *12*, 2492.

(15) Sun, X.; Li, W.; Wang, X.; Sui, Q.; Zhang, T.; Wang, Z.; Liu, L.; Li, D.; Feng, S.; Zhong, S.; Wang, H.; Bouchiat, V.; Nunez Regueiro, M.; Rougemaille, N.; Coraux, J.; Purbawati, A.; Hadj-Azzem, A.; Wang, Z.; Dong, B.; Wu, X.; Yang, T.; Yu, G.; Wang, B.; Han, Z.; Han, X.; Zhang, Z. Room Temperature Ferromagnetism in Ultra-Thin van Der Waals Crystals of 1*T*-$CrTe_2$. *Nano Res* **2020**, *13*, 3358–3363.

(16) Meng, L.; Zhou, Z.; Xu, M.; Yang, S.; Si, K.; Liu, L.; Wang, X.; Jiang, H.; Li, B.; Qin, P.; Zhang, P.; Wang, J.; Liu, Z.; Tang, P.; Ye, Y.; Zhou, W.; Bao, L.; Gao, H. J.; Gong, Y. Anomalous Thickness Dependence of Curie Temperature in Air-Stable Two-Dimensional Ferromagnetic 1*T*-$CrTe_2$ Grown by Chemical Vapor Deposition. *Nat Commun* **2021**, *12*, 809.

(17) Freitas, D. C.; Weht, R.; Sulpice, A.; Remenyi, G.; Strobel, P.; Gay, F.; Marcus, J.; Núñez-Regueiro, M. Ferromagnetism in Layered Metastable 1*T*-$CrTe_2$. *J. Phys.: Condens. Matter* **2015**, *27*, 176002.

(18) Huang, M.; Ma, Z.; Wang, S.; Li, S.; Li, M.; Xiang, J.; Liu, P.; Hu, G.; Zhang, Z.; Sun, Z.; Lu, Y.; Sheng, Z.; Chen, G.; Chueh, Y. L.; Yang, S. A.; Xiang, B. Significant Perpendicular Magnetic Anisotropy in Room-Temperature Layered Ferromagnet of Cr-Intercalated $CrTe_2$. *2D Mater* **2021**, *8*, 031003.

(19) Bensch, W.; Helmer, O.; Näther, C. Determination and redetermination of the crystal structures of chromium tellurides in the composition range $CrTe_{1.56}$–$CrTe_{1.67}$: Trigonal di-chromium tri-telluride Cr_2Te_3, monoclinic penta-chromium octa-telluride Cr_5Te_8, and the five layer superstructure of trigonal penta-chromium octa-telluride Cr_5Te_8. *Materials Research Bulletin* **1997**, *32*, 305-318.

(20) Kanazawa, N.; Seki, S.; Tokura, Y. Noncentrosymmetric Magnets Hosting Magnetic Skyrmions. *Adv. Mater.* **2017**, *29*, 1603227.

(21) Nagaosa, N.; Tokura, Y. Topological Properties and Dynamics of Magnetic Skyrmions. *Nature Nanotech* **2013**, *8*, 899–911.

(22) Wang, Y.; Yan, J.; Li, J.; Wang, S.; Song, M.; Song, J.; Li, Z.; Chen, K.; Qin, Y.; Ling, L.; Du, H.; Cao, L.; Luo, X.; Xiong, Y.; Sun, Y. Magnetic Anisotropy and Topological Hall Effect in the Trigonal Chromium Tellurides Cr_5Te_8. *Phys. Rev. B* **2019**, *100*, 024434.

(23) Dzyaloshinsky, I. A thermodynamic theory of “weak” ferromagnetism of antiferromagnetics. *Journal of Physics and Chemistry of Solids* **1958**, *4*, 241-255

(24) Moriya, T. Anisotropic superexchange interaction and weak ferromagnetism. *Phys. Rev.* **1960**, *120*, 91–98

(25) Saha, R.; Meyerheim, H. L.; Göbel, B.; Hazra, B. K.; Deniz, H.; Mohseni, K.; Antonov, V.; Ernst, A.; Knyazev, D.; Bedoya-Pinto, A.; Mertig, I.; Parkin, S. S. P. Observation of Néel-Type Skyrmions in Acentric Self-Intercalated $Cr_{1+\delta}Te_2$. *Nat Commun* **2022**, *13*, 3965.

(26) APEX4; Bruker AXS Inc.: Madison, Wisconsin, 2021.

(27) R.O. Diffraction, CrysAlis Pro, Rigaku Oxford Diffraction, Oxford, UK, 2018.

(28) Palatinus, L.; Chapuis, G. SUPERFLIP−a Computer Program for the Solution of Crystal Structures by Charge Flipping in Arbitrary Dimensions. *J. Appl. Crystallogr.* **2007**, *40*, 786−790.

(29) Petříček, V.; Dušek, M.; Palatinus, L. Crystallographic Computing System JANA2006: General features. Z. für Kristallogr. -Cryst. Mater. **2014**, *229*, 345−352.

(30) Denev, S. A.; Lummen, T. T. A.; Barnes, E.; Kumar, A.; Gopalan, V. Probing Ferroelectrics Using Optical Second Harmonic Generation. *J. Am. Ceram. Soc.* **2011**, *94*, 2699-2727.

(31) Shu, Z.; Wang, H.; Jo, N. H.; Jozwiak, C.; Bostwick, A.; Rotenberg, E.; Xie, W.; Kong, T. Synthesis and Physical Properties of a New Layered Ferromagnet $Cr_{1.21}Te_2$. *Phys. Rev. Mater.* **2023**, *7*, 044406.

32) Yan, J.; Luo, X.; Lin, G.; Chen, F.; Gao, J.; Sun, Y.; Hu, L.; Tong, P.; Song, W.; Sheng, Z.; Lu, W.; Zhu, X.; Sun, Y. Anomalous Hall Effect of the Quasi-Two-Dimensional Weak Itinerant Ferromagnet $Cr_{4.14}Te_8$. *EPL* **2018**, *124*, 67005.

(33) Liu, Y.; Abeykoon, M.; Stavitski, E.; Attenkofer, K.; Petrovic, C. Magnetic Anisotropy and Entropy Change in Trigonal Cr_5Te_8. *Phys. Rev. B* **2019**, *100*, 245114.

(34) Zhang, L. Z.; He, X. De; Zhang, A. L.; Xiao, Q. L.; Lu, W. L.; Chen, F.; Feng, Z.; Cao, S.; Zhang, J.; Ge, J. Y. Tunable Curie Temperature in Layered Ferromagnetic $Cr_{5+x}Te_8$ Single Crystals. *APL Mater* **2020**, *8*, 031101.

(35) Zhang, C.; Liu, C.; Zhang, J.; Yuan, Y.; Wen, Y.; Li, Y.; Zheng, D.; Zhang, Q.; Hou, Z.; Yin, G.; Liu, K.; Peng, Y.; Zhang, X. X. Room-Temperature Magnetic Skyrmions and Large Topological Hall Effect in Chromium Telluride Engineered by Self-Intercalation. *Adv. Mater.* **2023**, *35*, 2205967.

(36) Yang, Z.; Lange, M.; Volodin, A.; Szymczak, R.; Moshchalkov, V. V. Domain-Wall Superconductivity in Superconductor-Ferromagnet Hybrids. *Nat Mater* **2004**, *3*, 793–798.

(37) Tian, C. K.; Wang, C.; Ji, W.; Wang, J. C.; Xia, T. L.; Wang, L.; Liu, J. J.; Zhang, H. X.; Cheng, P. Domain Wall Pinning and Hard Magnetic Phase in Co-Doped Bulk Single Crystalline Fe_3GeTe_2. *Phys. Rev. B* **2019**, *99*, 184428.

(38) Wang, X. Y.; Xu, S.; Wang, H.; Lin, J. F.; Zeng, X. Y.; Ma, X. P.; Gong, J.; Wang, Y. T.; Han, K.; Xia, T. L. Uniaxial Magnetic Anisotropy and Anomalous Hall Effect in the Ferromagnetic Compound $PrMn_2Ge_2$. *Phys. Rev. B* **2023**, *107*, 144402.

(39) Winter, M.; Goncalves, F. J. T.; Soldatov, I.; He, Y.; Céspedes, B. E. Z.; Milde, P.; Lenz, K.; Hamann, S.; Uhlarz, M.; Vir, P.; König, M.; Moll, P. J. W.; Schlitz, R.; Goennenwein, S. T. B.; Eng, L. M.; Schäfer, R.; Wosnitza, J.; Felser, C.; Gayles, J.; Helm, T. Antiskyrmions and Their Electrical Footprint in Crystalline Mesoscale Structures of $Mn_{1.4}PtSn$. *Commun Mater* **2022**, *3*, 102.

(40) Wu, Y.; Zhang, S.; Zhang, J.; Wang, W.; Zhu, Y. L.; Hu, J.; Yin, G.; Wong, K.; Fang, C.; Wan, C.; Han, X.; Shao, Q.; Taniguchi, T.; Watanabe, K.; Zang, J.; Mao, Z.; Zhang, X.; Wang, K. L. Néel-Type Skyrmion in WTe_2/Fe_3GeTe_2 van Der Waals Heterostructure. *Nat Commun* **2020**, *11*, 3860.

(41) Chakraborty, A.; Srivastava, A. K.; Sharma, A. K.; Gopi, A. K.; Mohseni, K.; Ernst, A.; Deniz, H.; Hazra, B. K.; Das, S.; Sessi, P.; Kostanovskiy, I.; Ma, T.; Meyerheim, H. L.; Parkin, S. S. P. Magnetic Skyrmions in a Thickness Tunable 2D Ferromagnet from a Defect Driven Dzyaloshinskii–Moriya Interaction. *Adv. Mater.* **2022**, *34*, 2108637.

(42) Srivastava, A.K.; Devi, P.; Sharma, A. K.; Ma, T.; Deniz, H.; Meyerheim, H. L.; Felser, C.; Parkin, S. S. P. Observation of Robust Néel Skyrmions in Metallic PtMnGa. *Adv. Mater.* **2020**, *32*, 1904327.

(43) Nagaosa, N.; Sinova, J.;Onoda, S.; MacDonald, A. H.; Ong, N.P. Anomalous Hall effect. *Rev. Mod. Phys.* **2010**, *2*, 1539-1592.

(44) Liu, Y.; Petrovic, C. Anomalous Hall Effect in the Trigonal Cr_5Te_8 Single Crystal. *Phys. Rev. B* **2018**, *98*, 195122.

(45) Lee, M.; Onose, Y.; Tokura, Y.; Ong, N. P. Hidden Constant in the Anomalous Hall Effect of High-Purity Magnet MnSi. *Phys. Rev. B.* **2007**, *75*, 172403.

(46) Shiomi, Y.; Onose, Y.; Tokura, Y. Extrinsic Anomalous Hall Effect in Charge and Heat Transport in Pure Iron, $Fe_{0.997}Si_{0.003}$, and $Fe_{0.97}Co_{0.03}$. *Phys. Rev. B.* **2009**, *79*, 100404.

(47) Miyasato, T.; Abe, N.; Fujii, T.; Asamitsu, A.; Onoda, S.; Onose, Y.; Nagaosa, N.; Tokura, Y. Crossover Behavior of the Anomalous Hall Effect and Anomalous Nernst Effect in Itinerant Ferromagnets. *Phys. Rev. Lett.* **2007**, *99*, 086602.

(48) Iguchi, S.; Hanasaki, N.; Tokura, Y. Scaling of Anomalous Hall Resistivity in $Nd_2(Mo_{1-x}Nb_x)_2O_7$ with Spin Chirality. *Phys. Rev. Lett.* **2007**, *99*, 077202.

(49) Yang, S.-Y.; Wang, Y.; Ortiz, B. R.; Liu, D.; Gayles, J.; Derunova, E.; Gonzalez-Hernandez, R.; Šmejkal, L.; Chen, Y.; Parkin, S. S. P.; Wilson, S. D.; Toberer, E. S.; Mcqueen, T.; Ali, M. N. Giant, Unconventional Anomalous Hall Effect in the Metallic Frustrated Magnet Candidate, KV_3Sb_5. *Sci. Adv.* **2020**, *6*, eabb6003.

(50) Fujishiro, Y.; Kanazawa, N.; Kurihara, R.; Ishizuka, H.; Hori, T.; Yasin, F. S.; Yu, X.; Tsukazaki, A.; Ichikawa, M.; Kawasaki, M.; Nagaosa, N.; Tokunaga, M.; Tokura, Y. Giant Anomalous Hall Effect from Spin-Chirality Scattering in a Chiral Magnet. *Nat Commun* **2021**, *12*, 317

(51) Nakatsuji, S.; Kiyohara, N.; Higo, T. Large Anomalous Hall Effect in a Non-Collinear Antiferromagnet at Room Temperature. *Nature* **2015**, *527*, 212–215.

(52) Liu, E.; Sun, Y.; Kumar, N.; Muechler, L.; Sun, A.; Jiao, L.; Yang, S. Y.; Liu, D.; Liang, A.; Xu, Q.; Kroder, J.; Süß, V.; Borrmann, H.; Shekhar, C.; Wang, Z.; Xi, C.; Wang, W.; Schnelle, W.; Wirth, S.; Chen, Y.; Goennenwein, S. T. B.; Felser, C. Giant Anomalous Hall Effect in a Ferromagnetic Kagome-Lattice Semimetal. *Nat Phys* **2018**, *14*, 1125–1131.

(53) Kanazawa, N.; Onose, Y.; Arima, T.; Okuyama, D.; Ohoyama, K.; Wakimoto, S.; Kakurai, K.; Ishiwata, S.; Tokura, Y. Large Topological Hall Effect in a Short-Period Helimagnet MnGe. *Phys. Rev. Lett.* **2011**, *106*, 156603.

(54) Takahashi, K. S.; Ishizuka, H.; Murata, T.; Wang, Q. Y.; Tokura, Y.; Nagaosa, N.; Kawasaki, M. Anomalous Hall Effect Derived from Multiple Weyl Nodes in High-Mobility $EuTiO_3$ Films. *Sci. Adv.* **2018**, 4, eaar7880.

(55) Leroux, M.; Stolt, M. J.; Jin, S.; Pete, D. V.; Reichhardt, C.; Maiorov, B. Skyrmion Lattice Topological Hall Effect near Room Temperature. *Sci Rep* **2018**, *8* (1), 15510.

(56) Kurumaji, T.; Nakajima, T.; Hirschberger, M.; Kikkawa, A.; Yamasaki, Y.; Sagayama, H.; Nakao, H.; Taguchi, Y.; -Hisa Arima, T.; Tokura, Y. Skyrmion Lattice with a Giant Topological Hall Effect in a Frustrated Triangular-Lattice Magnet. *Science* **2019**, *365*(6456), 914-918.

(57) Raju, M.; Petrović, A. P.; Yagil, A.; Denisov, K. S.; Duong, N. K.; Göbel, B.; Şaşıoğlu, E.; Auslaender, O. M.; Mertig, I.; Rozhansky, I. V.; Panagopoulos, C. Colossal Topological Hall

Effect at the Transition between Isolated and Lattice-Phase Interfacial Skyrmions. *Nat Commun* **2021**, *12* (1), 2758.

(58) Chakraborty, A.; Srivastava, A. K.; Sharma, A. K.; Gopi, A. K.; Mohseni, K.; Ernst, A.; Deniz, H.; Hazra, B. K.; Das, S.; Sessi, P.; Kostanovskiy, I.; Ma, T.; Meyerheim, H. L.; Parkin, S. S. P. Magnetic Skyrmions in a Thickness Tunable 2D Ferromagnet from a Defect Driven Dzyaloshinskii–Moriya Interaction. *Adv. Mater.* **2022**, *34*, 2108637.

(59) Li, Z.; Zhang, H.; Li, G.; Guo, J.; Wang, Q.; Deng, Y.; Hu, Y.; Hu, X.; Liu, C.; Qin, M.; Shen, X.; Yu, R.; Gao, X.; Liao, Z.; Liu, J.; Hou, Z.; Zhu, Y.; Fu, X. Room-temperature sub-100 nm Néel-type skyrmions in non-stoichiometric van der Waals ferromagnet $Fe_{3-x}GaTe_2$ with ultrafast laser writability. *Nat Commun* **2024**, *15*, 1017.

(60) Ma, T.; Sharma, A. K.; Saha, R.; Srivastava, A. K.; Werner, P.; Vir, P.; Kumar, V.; Felser, C.; Parkin, S. S. P. Tunable Magnetic Antiskyrmion Size and Helical Period from Nanometers to Micrometers in a D_{2d} Heusler Compound. *Adv. Mater.* **2020**, *32*, 2002043.

(61) Raju, M.; Petrović, A. P.; Yagil, A.; Denisov, K. S.; Duong, N. K.; Göbel, B.; Şaşıoğlu, E.; Auslaender, O. M.; Mertig, I.; Rozhansky, I. V.; Panagopoulos, C. Colossal Topological Hall Effect at the Transition Between Isolated and Lattice-phase Interfacial Skyrmions. *Nat Commun* **2021**, *12*, 2758.

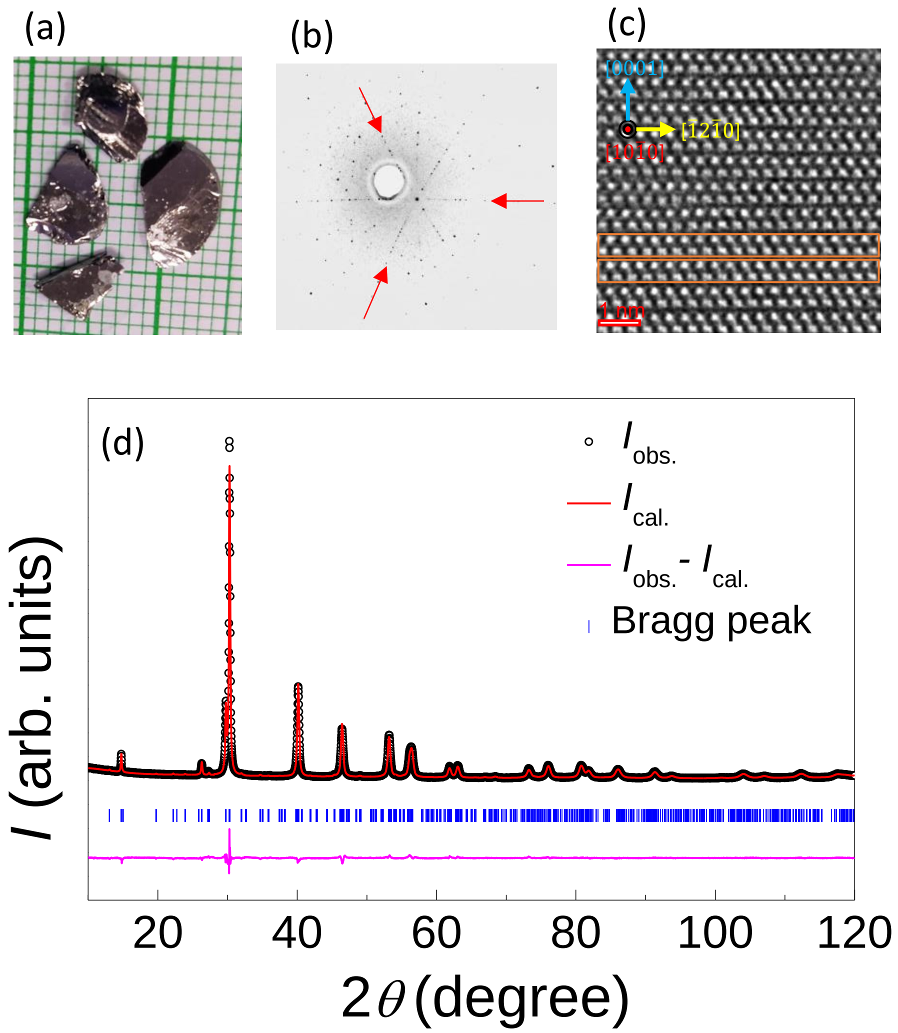

Fig. 1. Structural characterisation of tr-Cr_5Te_8. (a) Image of as-grown single crystals of tr-Cr_5Te_8. (b) Laue diffraction pattern of tr-Cr_5Te_8 single crystal along [0001] direction. Red arrows show the three-fold symmetric points. (c) High resolution transmission electron microscopy (HRTEM) image of tr-Cr_5Te_8 viewed along [$10\bar{1}0$] direction. The Cr-Te-Cr triple layers are highlighted with the saffron rectangles. (d) Rietveld refinement of PXRD data of tr-Cr_5Te_8 refined with $P3m1$ space group. The refinement parameters are as follow: *R(obs)*= 2.51, *wR(obs)*= 3.61, *R(all)*= 3.12, *wR(all)*= 3.73; GOF= 1.96, *Rp*= 3.96, *wRp*= 5.18.

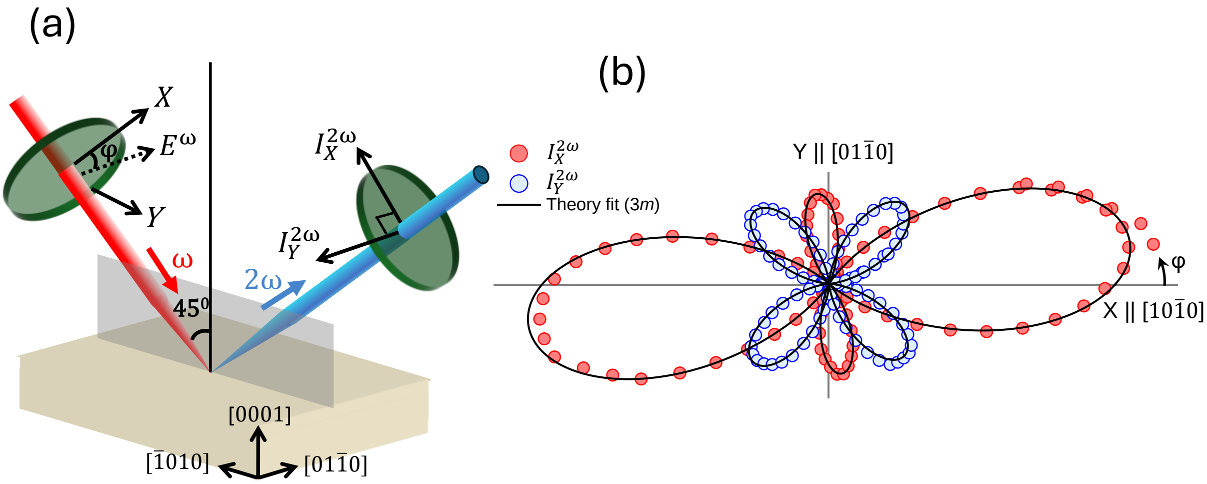

Fig. 2. Second harmonic generation (SHG) in tr-Cr_5Te_8. (a) Schematic of the SHG setup used for measurements. An 800 nm fundamental wavelength is used to generate 400 nm second harmonic light. The angle of incidence of measurement is 45°. φ denotes the angle of polarization of the incident beam. (b) Measured SHG polar plots as a function of incident polarization angle (φ) of the fundamental beam corresponding to two orthogonal directions of SHG detection ($I_X^{2\omega}$ (red), $I_Y^{2\omega}$ (blue)). Solid lines indicate the polar plot fitting to point group $3m$ model.

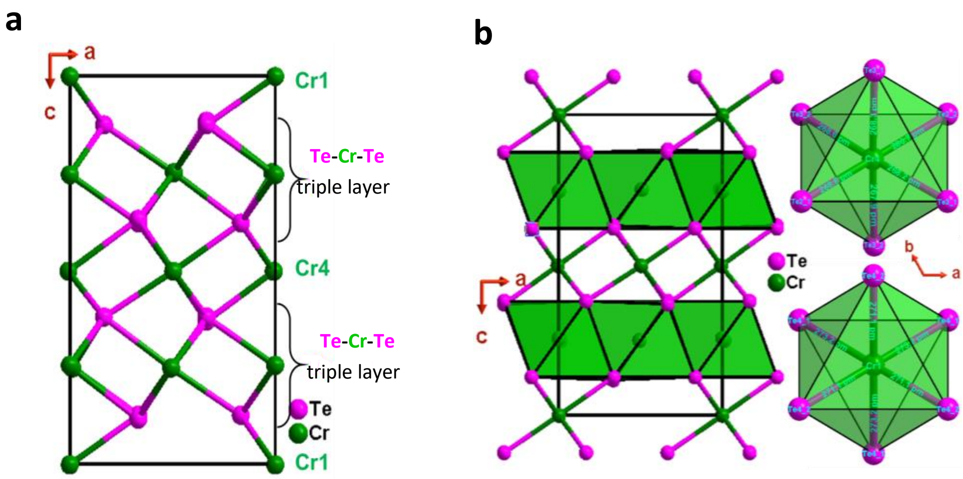

Fig. 3. Crystal structure of tr-Cr_5Te_8. (a) Alternate layers of Cr and Te in the unit cell of tr-Cr_5Te_8. (f) Stuffed CdI_2-type tr-Cr_5Te_8.

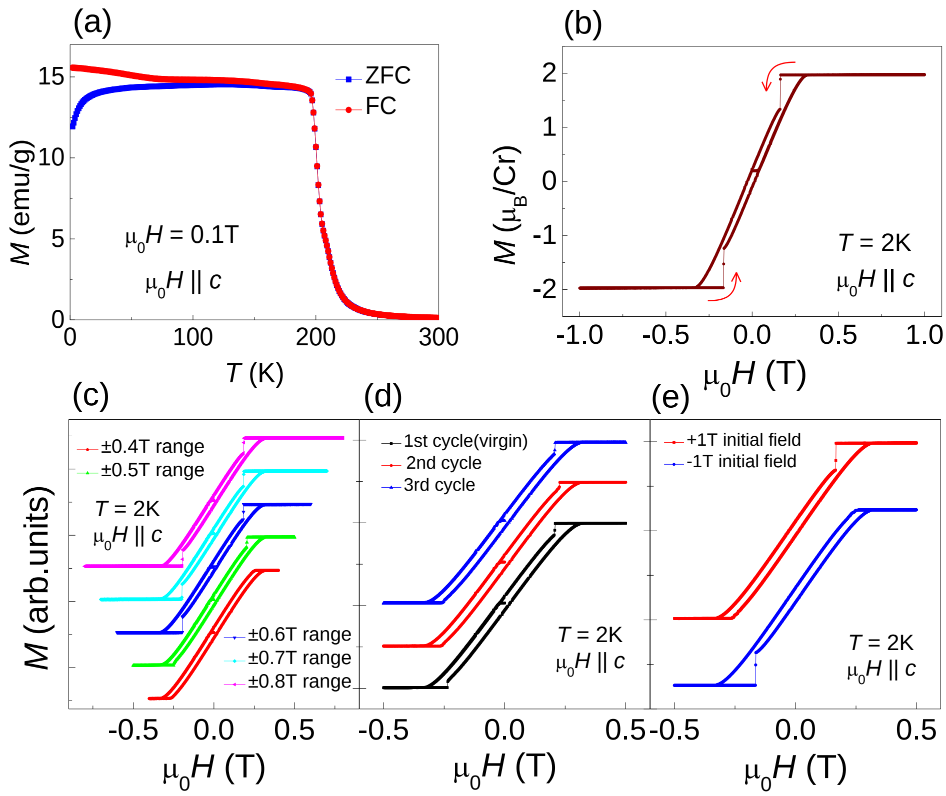

Fig. 4. Magnetic properties of tr-Cr_5Te_8 with magnetic field applied along the *c*-axis. (a) Temperature dependence of the magnetisation (*M*) under ZFC and FC conditions. The inset shows the temperature dependence of the first derivative of *M*. (b)-(e) Magnetic field dependence of the magnetisation at temperature 2 K (b) for field range of ±1 T (arrows show the direction of field sweep.) (c) for field ranges ±0.4 T, ±0.5 T, ±0.6 T, ±0.7 T and ±0.8 T (d) for the sample cooled at zero field (three consecutive hysteresis are shown) (e) for the sample exposed to +1T/-1T initial field (red/blue).

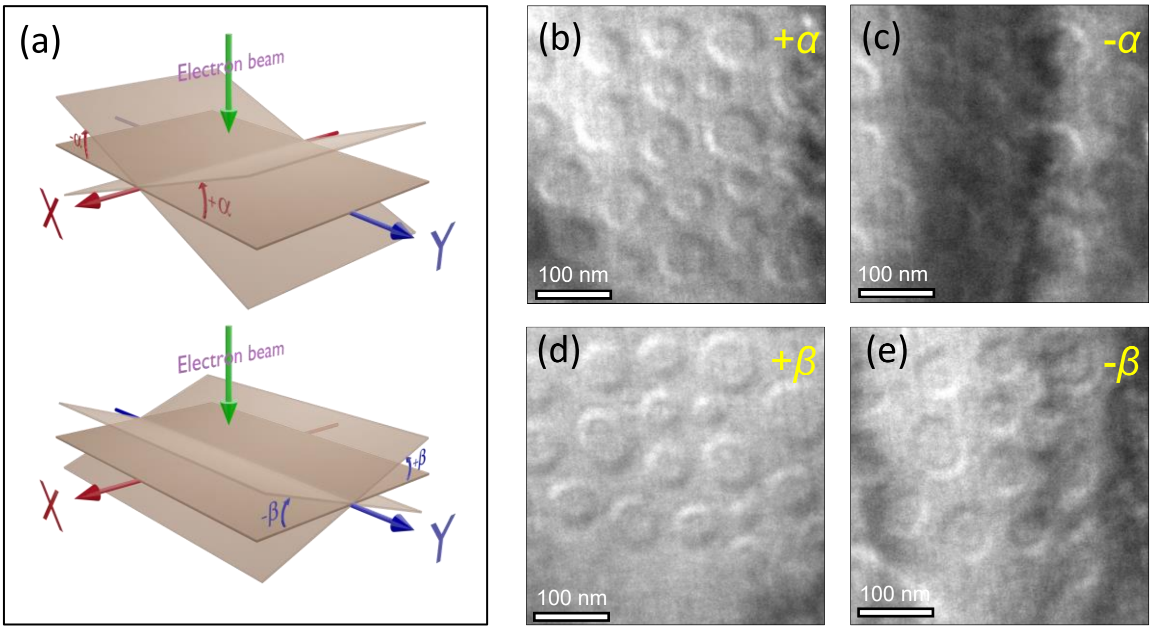

Fig. 5. LTEM images of Néel type skyrmions in tr-Cr_5Te_8 at temperature 100 K in zero magnetic field. (a) Definition of tilt angles α, β and the corresponding X and Y tilt axes. LTEM images for the tilt angle of (b)-(c) α=$\pm15^{\mathrm{O}}$ and (d)-(e) β=$\pm15^{\mathrm{O}}$.

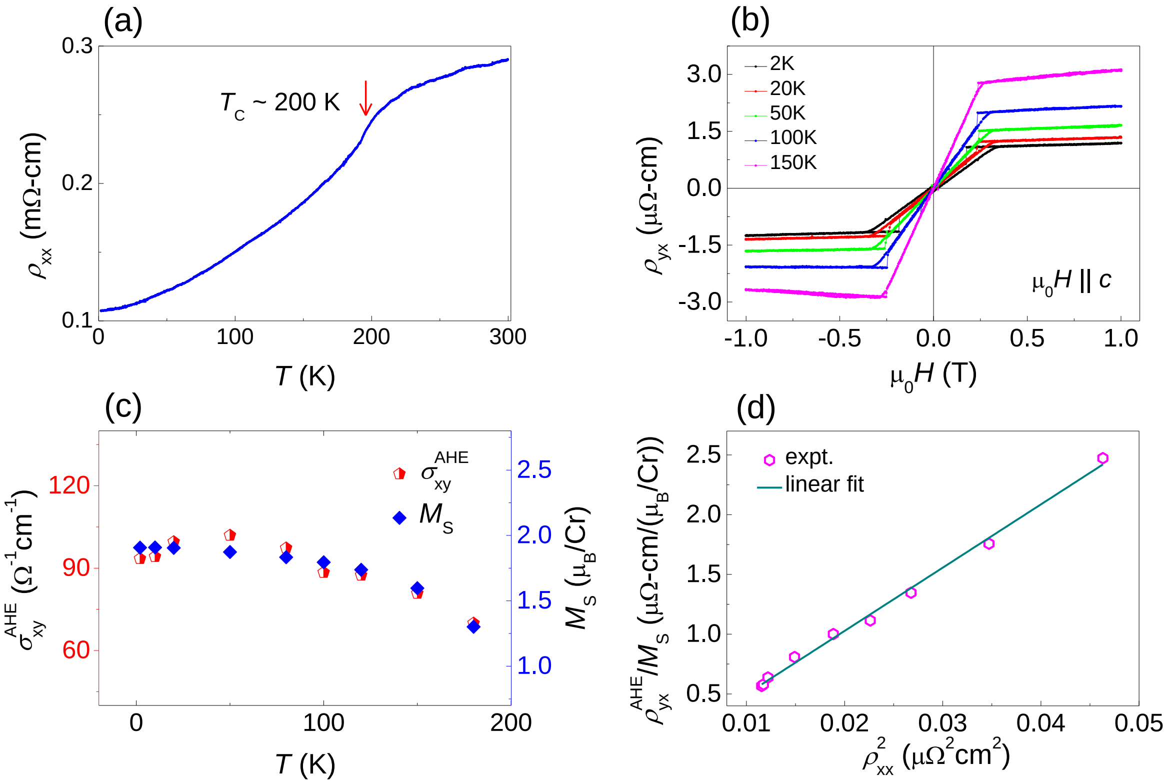

Fig. 6. Transport properties of tr-Cr_5Te_8. (a) Temperature dependence of the longitudinal resistivity (ρ_{xx}). (b) Field dependence of the Hall resistivity (ρ_{xy}) at various temperatures with field applied along the *c*-axis. (c) Variation of anomalous Hall conductivity as a function of temperature. (d) Scaling of anomalous Hall resistivity with the longitudinal resistivity. The green line is the linear fit of the data.

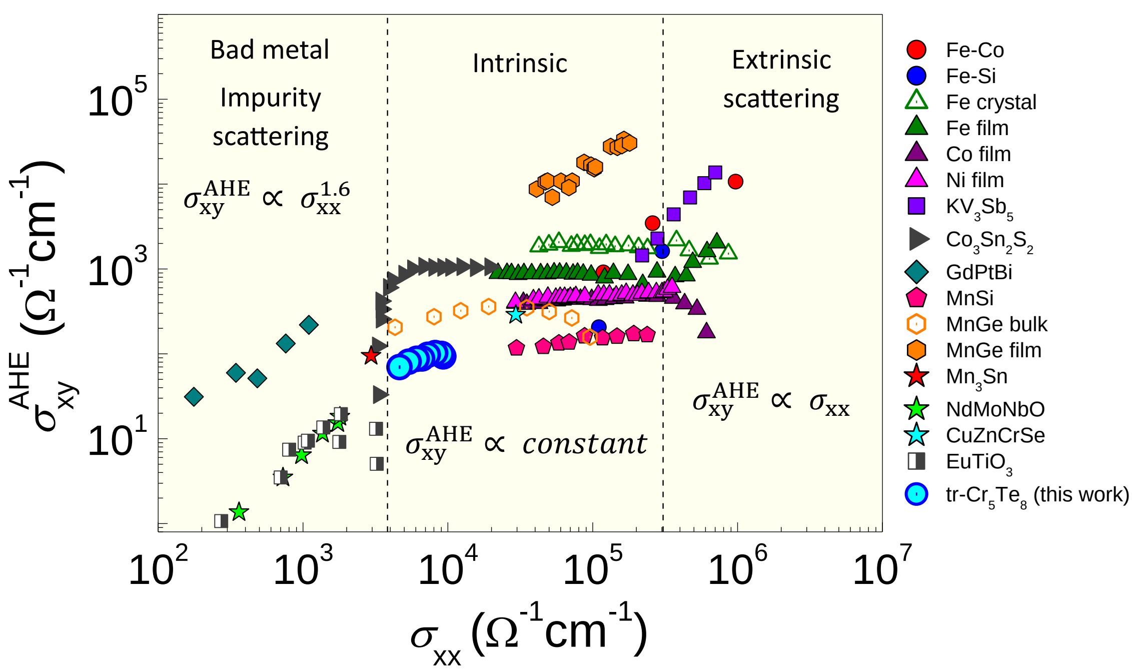

Fig. 7. Dependence of σ_{xy}^{AHE} with σ_{xx} for various materials taken from the literature along with the data of tr-Cr_5Te_8.

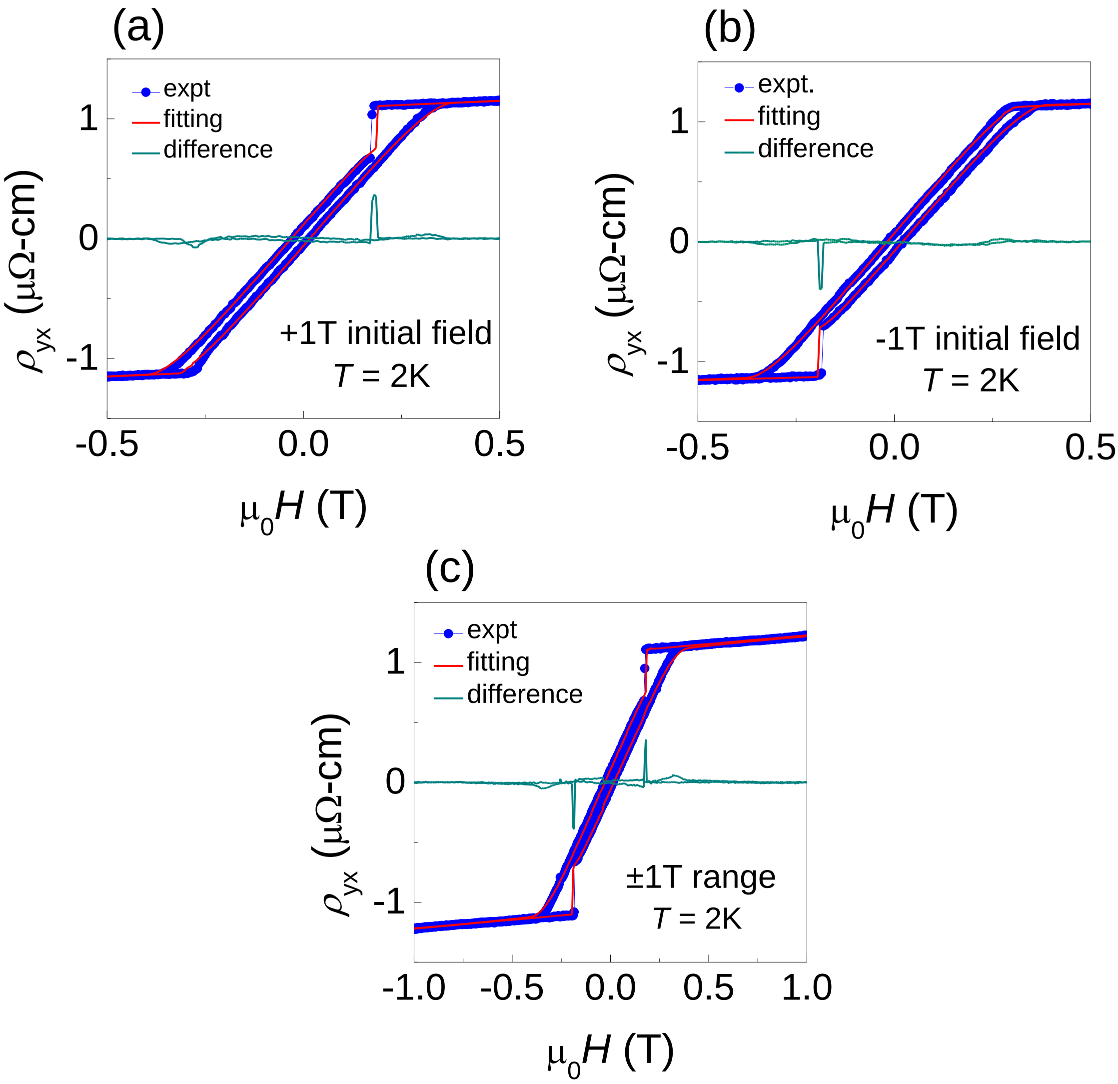

Fig. 8. Estimation of the topological Hall component when the hump in Hall data and magnetization appears in (a) positive magnetic field, (b) negative magnetic field and (c) both positive and negative magnetic field.